Supplementary Figures

Fig. S1. Marker gene expression used to curate annotations within the terminal ileum atlas.

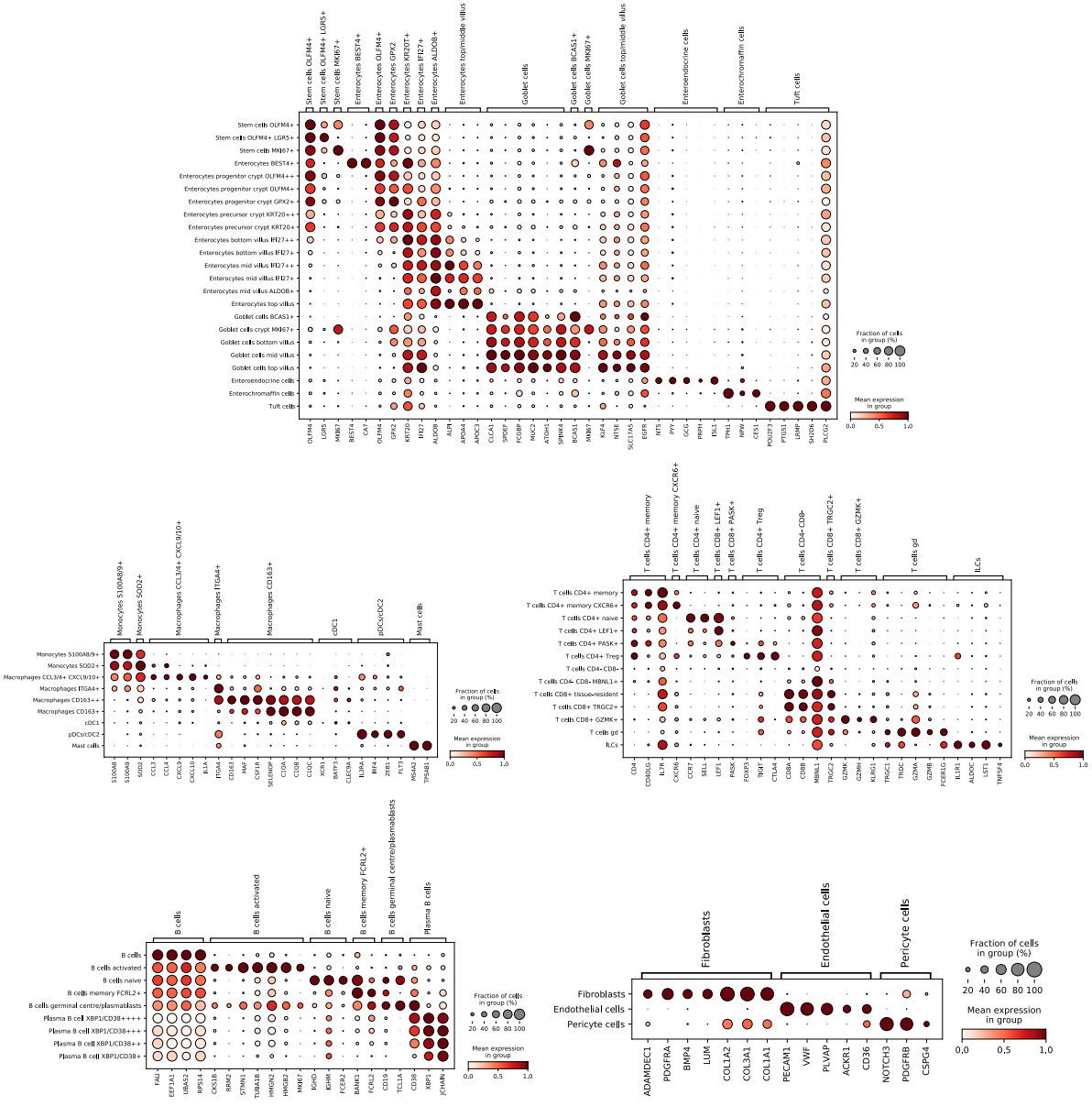

Transcriptional signatures based on literature-derived or expert-curated markers were used to define epithelial, myeloid, T cell, B cell, plasma B cell, and mesenchymal cell types. Dot size indicates the proportion of cells within each cluster expressing a specific marker, color intensity reflects the mean expression of the gene within the cluster.

Fig. S2. Epithelial cell types represent the crypt-villus axis differentiation.

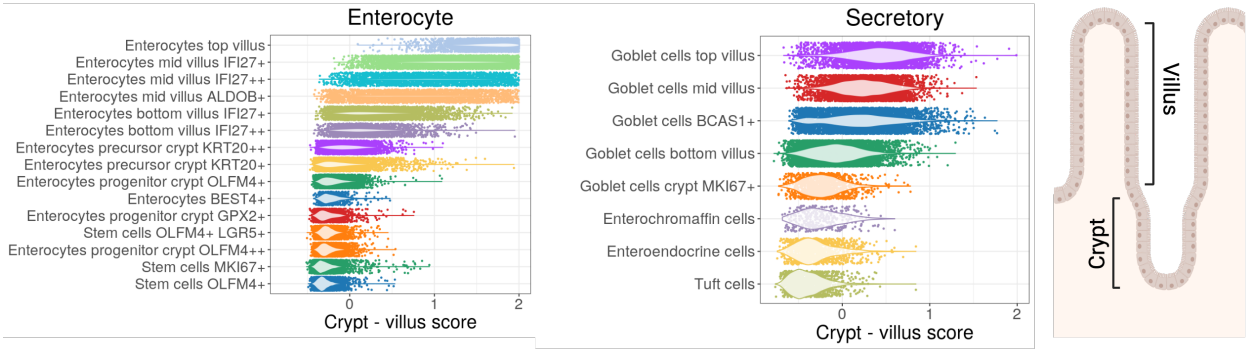

Spatial distribution of enterocytes and secretory cells along the crypt-villus axis was inferred using gene signatures from Moor et al. (2018) (Methods). A subset of enterocytes, termed “top villus enterocytes,” exhibited elevated expression scores for a specific gene signature (including *APOA4, APOC3, ALPI*), indicative of cells located at the villus tip. In contrast, enterocytes situated along the mid-villus or in progenitor/stem cell zones showed lower expression of these markers. Similarly, goblet cells were evaluated for a top-villus gene signature comprising *EGFR, KLF4 and NT5E*. Top villus goblet cells demonstrated slightly higher expression scores compared to goblet cells in mid-villus regions and those at the crypt base.

Fig. S3. Cell-type proportions across healthy and CD samples in the atlasing cohort.

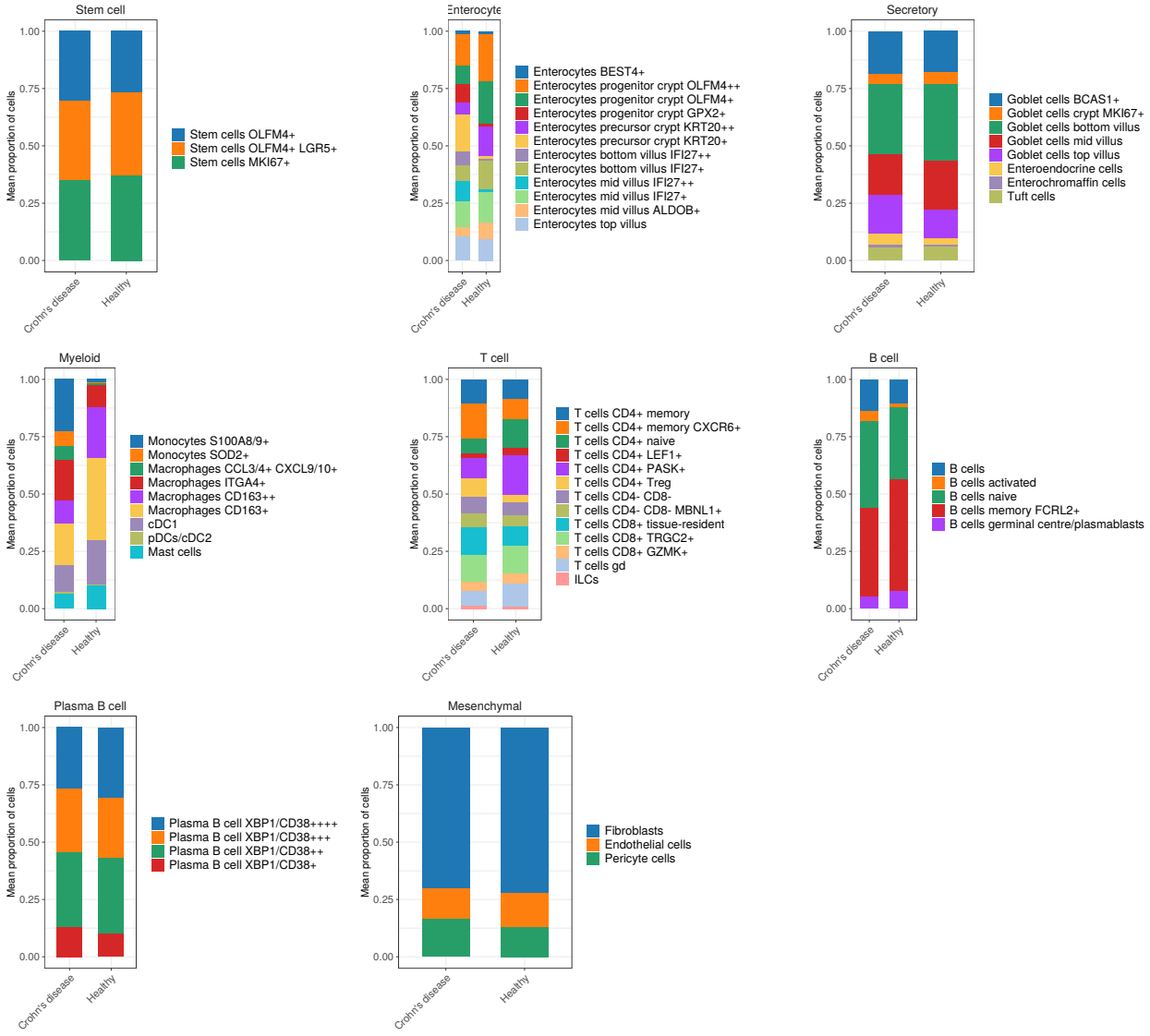

Compositional differences in cell-type proportions between CD patients (n=25) and healthy controls (n=35) across eight major cell populations.

Fig. S4. Concordance of gene specificities across discovery and replication datasets.

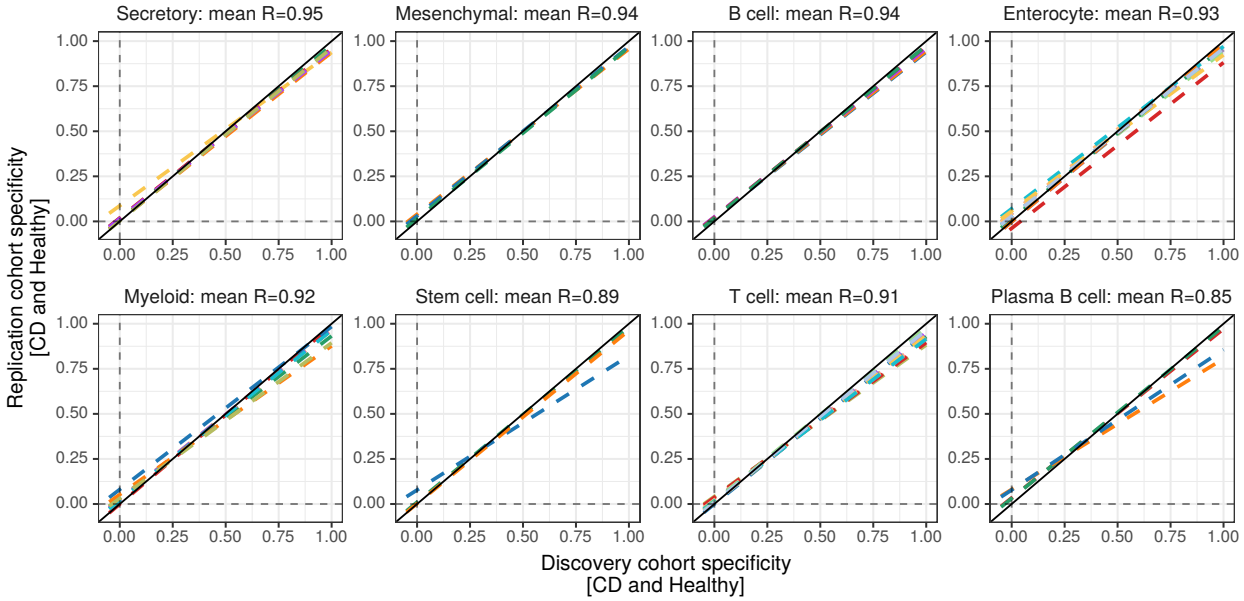

Linear regression model between computationally determined, specifically expressed genes (without thresholding, as outlined in Methods) in the discovery dataset (n=171, x-axis) and replication dataset (n=172, y-axis). For the color legend, please refer to Fig. 1b. The reported mean R represents the average of regression coefficients calculated across cell types within each major cell population.

Fig. S5. Accuracy in re-annotating the atlas cohort.

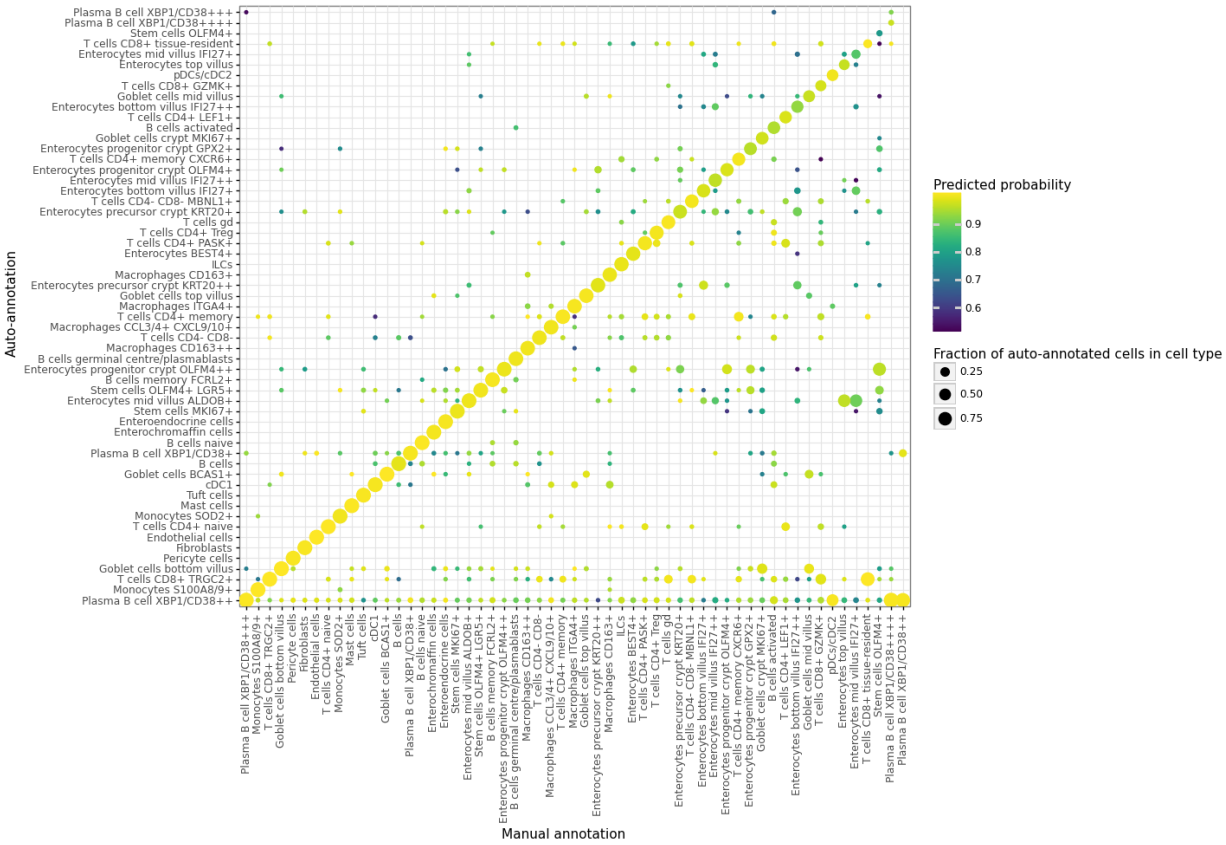

Dot size represents the proportion of auto-annotated cells in the atlas cohort (n=70, y-axis) within each manually defined cluster (x-axis), with color indicating the probability of the mapping prediction.

Fig. S6. Differentially expressed genes between CD inflamed and healthy samples across all 57 cell types.

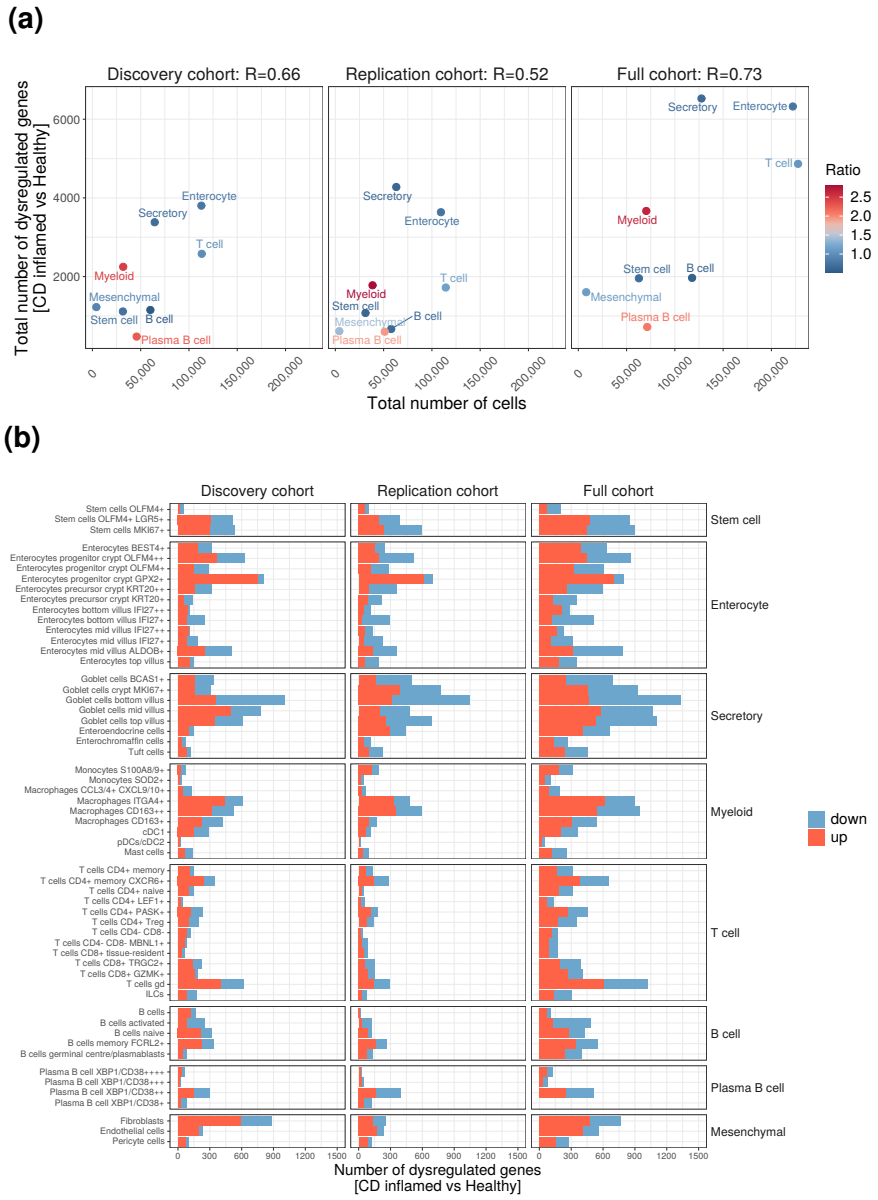

(a) The total number of cells in each major cell population (x-axis), the total number of significantly dysregulated genes (FDR $<$ 5%), and the ratio of cells in CD versus healthy controls (color-coded) across the discovery, replication, and full cohorts. Pearson correlation coefficients (R) were calculated for all major cell populations. **(b)** The number of significantly up- and down-regulated genes (FDR $<$ 5%) is shown on the x-axis for each of the 57 cell types (y-axis) across the discovery, replication, and full cohorts.

Fig. S7. Dysregulated pathways in CD versus healthy epithelial cells.

(a) MHC-I antigen presentation

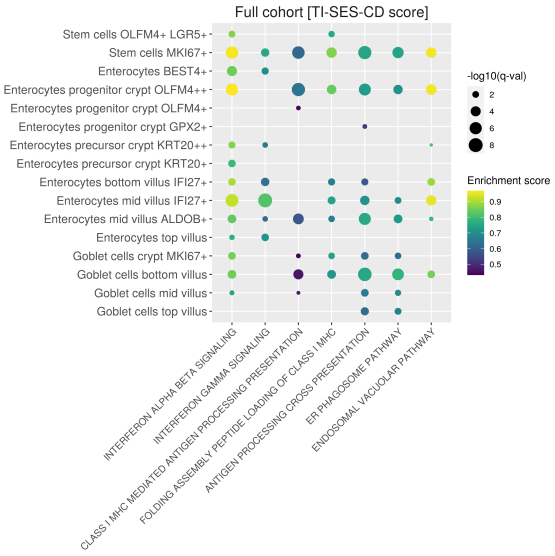

(b) MHC-I vs MHC-II antigen presentation

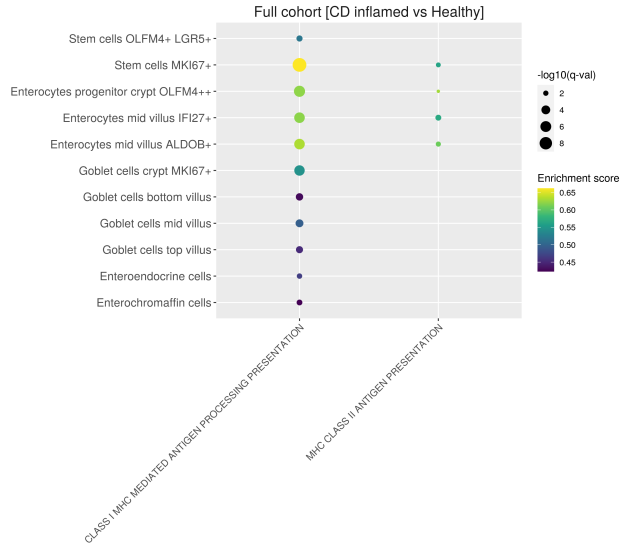

(c) Metabolic pathways

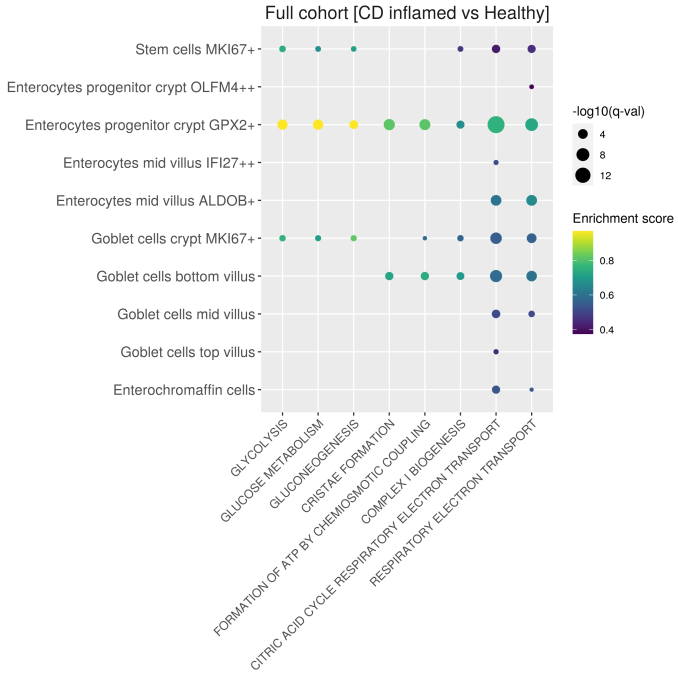

Gene set enrichment analysis was conducted on z-scores derived from the differential gene expression hurdle model applied to the full cohort. The results reveal upregulated pathways in CD epithelial cells, including **(a)** those associated with the TI-SES-CD score, **(b)** enrichment of MHC class II antigen presentation compared to MHC class I, and **(c)** significant metabolic changes within epithelial cells. Populations exhibiting low fold-change replicability ($R < 0.5$, Table S5) were excluded from this analysis.

Fig. S8. Myeloid cell types enriched for CD heritability are found predominantly in CD gut biopsies.

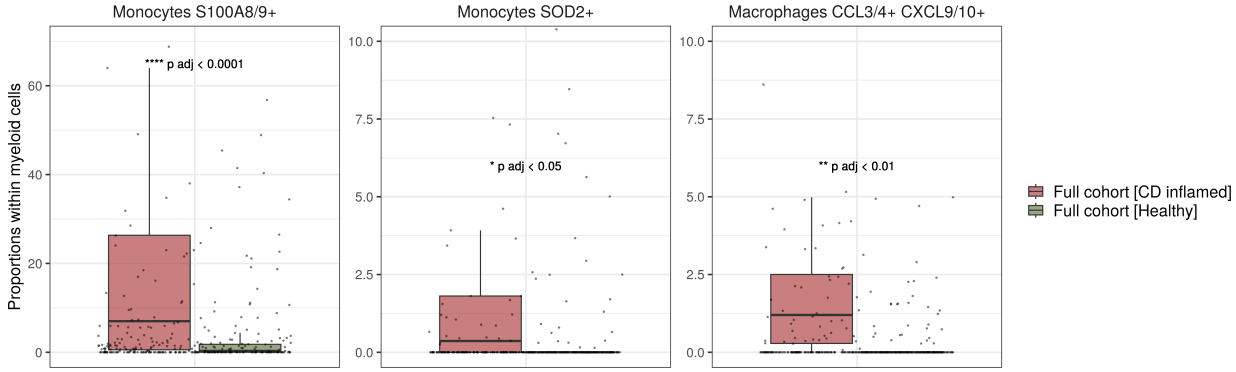

Boxplots show statistical significance (t-test) in the proportions of *S100A8/9+* and *SOD2+* monocytes and *CCL3/4+ CXCL9/10+* macrophages within myeloid cells, comparing inflamed CD and healthy samples.

Fig. S9. Optimisation of cluster resolution for cell-type identification.

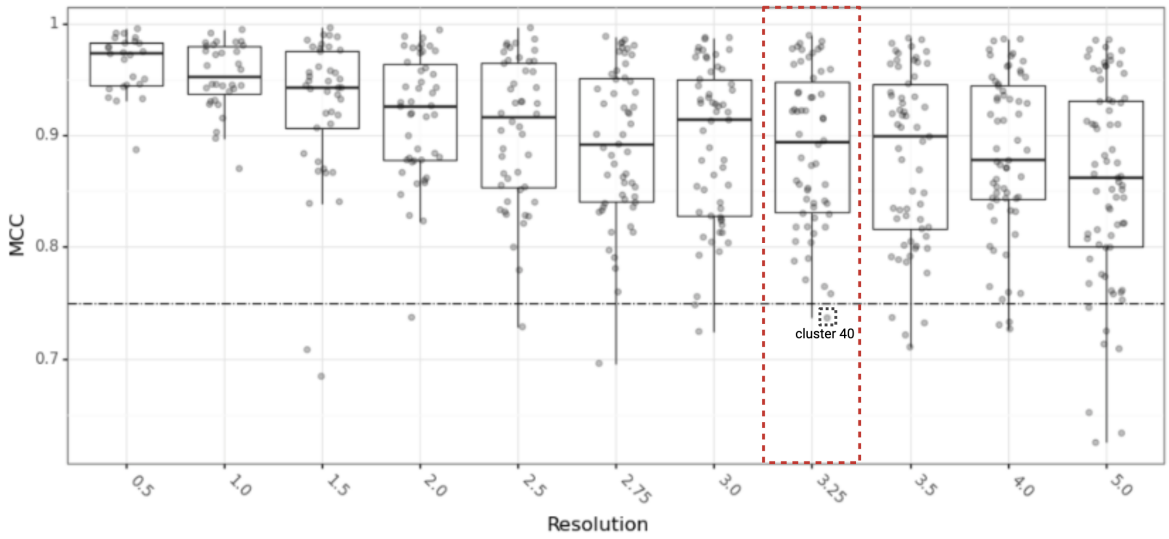

Cluster predictability (x-axis) across a range of clustering resolutions (y-axis). Cluster predictability was assessed by training a keras model on 2/3 of data and calculating the matthews correlation coefficient (MCC) in the remaining 1/3 test set (Methods). A resolution of 3.25 was selected, as cluster predictability rapidly declined at resolutions greater than 3.25. At this resolution, all clusters met the MCC threshold of $>$ 0.75, with the exception of cluster 40, which exhibited an MCC $<$ 0.75 at multiple resolutions and was therefore excluded.

Supplementary Tables

Table S3. Demographics of healthy and disease samples across cohorts.

	Discovery (%)	Replication (%)	P-value
N	171	172	
Disease status = Crohn's Disease	57 (33.3)	54 (31.4)	0.730
Inflamed	29 (17.0)	35 (20.3)	0.489
Sex = M	82 (48.0)	84 (48.8)	0.914
Mean age (SD)	46.62 (14.05)	46.49 (12.98)	0.928

Absolute number and proportions of demographics across discovery and replication cohorts. Non-significant differences determined by Fisher's exact test or t-test (for age). SD=standard deviation.